Advanced Engineering Materials

ADVANCED ENGINEERING MATERIALS
www.aem-journal.com

RESEARCH ARTICLE OPEN ACCESS

Thermomechanical Fatigue and Creep–Fatigue Interaction of Inconel 718 Additively Manufactured by Laser Beam Powder Bed Fusion

Stefan Guth[1] | Tomáš Babinský[2] | Jan Lars Riedel[1] | Wen Hao Kan[3] | Aijun Huang[4] | Martin Heilmaier[1] | Ivo Šulák[5]

[1]Karlsruhe Institute of Technology, Institute for Applied Materials, Engelbert-Arnold-Straße 4, Karlsruhe, Germany | [2]Paul Scherrer Institute, Forschungsstraße 111, Villigen, Switzerland | [3]Sydney Manufacturing Hub, The University of Sydney, Camperdown, Australia | [4]Monash University, Monash Center for Additive Manufacturing, 15–17 Normanby Rd., Notting Hill, Australia | [5]Institute of Physics of Materials, Czech Academy of Sciences, Žižkova 22, Brno, Czech Republic

Correspondence: Stefan Guth (stefan.guth@kit.edu)

Received: 6 October 2025 | **Revised:** 12 January 2026 | **Accepted:** 29 January 2026

Keywords: additive manufacturing | creep–fatigue interaction | Inconel 718 | laser beam powder bed fusion (PBF-LB) | thermo-mechanical fatigue

ABSTRACT

This study investigates the Ni-based superalloy Inconel 718 produced by laser beam powder bed fusion (PBF-LB) under thermomechanical fatigue (TMF) loading. Strain-controlled TMF tests under in-phase and out-of-phase conditions were conducted in the temperature range from 300°C to 650°C. To increase creep–fatigue interaction, tensile dwell times of 10 min at 650°C were introduced in some in-phase TMF tests. After hot isostatic pressing, solution annealing and age-hardening, the PBF-LB material recrystallized and exhibited finely dispersed γ'' precipitates, typical of Inconel 718. In this state, the material showed a cyclic deformation behavior comparable to that of conventionally-rolled Inconel 718. In tests without dwell times, the TMF lifetimes of PBF-LB Inconel 718 reached almost those of conventionally-rolled Inconel 718. Introducing dwell times significantly reduced the TMF life of PBF-LB Inconel 718. The results suggest that this effect can be attributed to a lack of grain boundary precipitates, which may facilitate grain boundary sliding and promote intergranular crack propagation.

1 | Introduction

Creep–fatigue interaction is often a critical factor limiting the service life of high-temperature components, e.g., in gas turbines or jet engines. In these hot-operating systems, start-up, load-change, and shut-down operations induce thermomechanical fatigue (TMF) loading where the materials face both thermal and mechanical cycling. A thorough understanding of the damage and deformation mechanism under TMF loading is essential for reliable and resource-efficient design of high-temperature components. Depending on the TMF phase angle between mechanical load and temperature, the amount of creep–fatigue interaction varies [1–3]. The most detrimental phase angles are usually 0° (in-phase, IP), representing the loading situation on local cold spots, e.g., in cooling channels, and 180° (out-of-phase, OP), representative of local hot spots. Creep–fatigue interaction is most significant for IP loading because peak tensile strain and stress coincide with the highest temperature. For polycrystalline materials, this favors intergranular damage due to cavity formation [4] and grain boundary sliding [5–7]. Therefore, IP loading often represents the most detrimental TMF phase angle [1, 3, 8, 9]. In OP loading, intergranular damage is largely suppressed since compressive strain and stress occur during the high-temperature part of the cycle. However, plastic creep deformation under compressive stress may increase the tensile stress in the following cycle, which accelerates crack propagation and reduces the lifetime [3, 10]. Steady-state operation at high temperatures, which can be represented in laboratory tests by dwell times, intensifies creep–fatigue interaction under both IP- and OP-TMF conditions, typically resulting in reduced lifetimes [11–13].

Inconel 718 is a Ni-based superalloy, which is widely used in high-temperature applications thanks to its excellent resistance to creep, fatigue, and oxidation. Its fcc γ-matrix is strengthened by coherently embedded precipitates of the γ'' phase (Ni_3Nb) and, to a lesser extent, the γ' phase ($Ni_3(Al, Ti)$), resulting in outstanding high-temperature strength up to about 650°C. For temperatures above 650°C, the metastable γ'' phase transforms into the stable δ phase, leading to a significant decrease in tensile and yield strength. Conventional fabrication methods of Inconel 718 are forging, casting, and powder metallurgy. Inconel 718 produced by these established methods has been the focus of numerous studies, thereby providing a solid understanding of the alloy's creep-fatigue and TMF behavior [8, 14–17]. Owing to its good weldability, Inconel 718 is also frequently fabricated using additive manufacturing (AM) techniques. These enable not only unprecedented design freedom but also new means of microstructural control. Powder bed fusion processes utilizing laser beam (PBF-LB) or electron beam (PBF-EB) can produce Inconel 718 microstructures with distinct grain morphologies, textures [18], and precipitation structures, which are difficult or impossible to obtain by conventional processing routes. The microstructural differences of AM Inconel 718 may increase the alloy's TMF and creep-fatigue resistance. A recent study conducted by several authors of the present work demonstrated that PBF-EB Inconel 718 outperforms conventionally-rolled Inconel 718 in strain-controlled IP-TMF tests, primarily due to a low elastic modulus along the build direction, resulting in reduced stresses [19]. Although PBF-LB Inconel 718 has been extensively studied in the last decade [20–25], there are only a few studies addressing the TMF and creep-fatigue behavior. Popovich et al. found for IP-TMF loading with a temperature range of 350°C–650°C and 300 s dwell times at 650°C that a solution annealing and aging treatment increases the lifetime by a factor of two when compared to the as-built state. They explained this effect with δ-phase particles precipitating at grain boundaries during the heat treatment, which restricts grain boundary sliding [26]. Zou et al. compared the TMF behavior of PBF-LB Inconel 718 under both IP and OP conditions with the isothermal fatigue behavior at various temperatures. Similar to conventionally-rolled Inconel 718, they found that TMF loading results in shorter lifetimes than isothermal loading at the maximum temperature of the TMF cycle. Furthermore, IP-TMF loading was found to be more detrimental than OP-TMF loading [27]. In this study, we aim to highlight both the potential and the limitations of PBF-LB Inconel 718 for high temperature applications involving severe creep–fatigue interaction. Therefore, we performed TMF tests on PBF-LB Inconel 718 under IP and OP conditions with a temperature range of 300–650°C and optional dwell times of 600s at 650°C. The results are compared with those of conventionally-rolled and PBF-EB Inconel 718, as partially reported in a previous study [19].

2 | Experimental Section

2.1 | Material and Specimen Manufacturing

A General Electric Concept Laser XLINE 2000R PBF-LB system was applied to fabricate cylindrical Inconel 718 rods of 80 mm length and 20 mm diameter. The building direction was parallel to the cylinder axis (standing specimens). The applied laser power was 285 W with a scanning speed of 960 mm s^{-1}, a layer thickness of 50 µm, a hatch spacing of 110 µm, and a trace width of 200 µm. The island scan strategy with an island of 10 mm × 10 mm was used. From the PBF-LB rods, solid round fatigue testing specimens with a cylindrical gauge length of 10 mm and a gauge length diameter of 4.5 mm were machined using a CNC-controlled lathe. Figure 1a schematically shows how the fatigue specimens were extracted from the PBF-LB rods. For all tested specimens, the loading axis was parallel to the building direction (0° specimens). Figure 1b shows the fatigue specimen dimensions. The final machining step was fine-turning to reach the specified Ra values of 0.4 µm.

Initially, the specimens were intended for heat treatment after machining and then testing. However, in order to enable comparison with PBF-EB Inconel 718 specimens, which were hot isostatically pressed (HIPed) [28], an identical postmachining HIP step at 1120°C and 100 MPa for 4 h was applied to the PBF-LB specimens. This sequence may influence surface-sensitive properties and is discussed later accordingly. Some comparative TMF tests were conducted on conventionally-rolled (used synonymously to conventional) Inconel 718, which was already used in a previous study [19]. Further details on these specimens with identical geometry as the PBF-LB specimens can be found there. The chemical composition of the specimens, as determined by optical emission spectroscopy using a Spectrolab M10 device, is shown in Table 1. The PBF-LB specimens exhibit an approximately 1% higher Cr concentration and a 1% lower Fe concentration than the conventional specimens. The other element concentrations match closely. Before testing, all specimens were solution annealed at 1065°C for 2 h, followed by two-stage aging at 718°C and 621°C for 8 h each. To avoid oxidation, the heat treatments were performed in a vacuum furnace. The heat treatment of the specimens was identical to that performed on conventionally-rolled and PBF-EB -manufactured Inconel 718 specimens that were TMF-tested in the above-mentioned previous study [19].

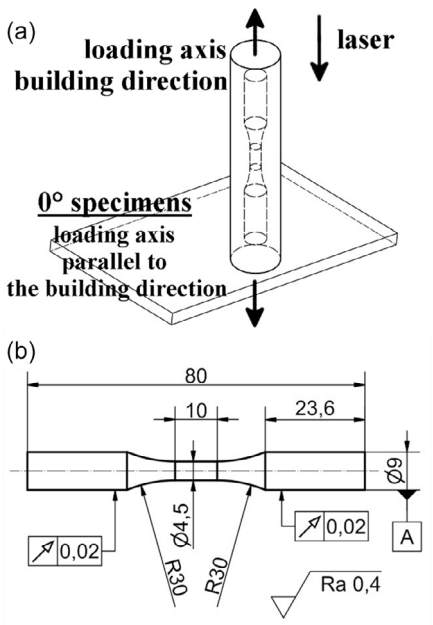

FIGURE 1 | PBF-LB fatigue testing specimens. (a) Schematic showing the specimen orientation relative to the building direction of the PBF-LB rods. (b) Dimensions of the specimens given in mm (Ra in µm).

TABLE 1 | Chemical composition of specimens in wt.%.

	C	Cr	Mo	Nb	Ti	Al	Fe	Ni
PBF-LB Inconel 718	0.04	19.4	2.9	4.7	0.89	0.57	17.7	Bal.
Conventional Inconel 718	0.03	18.3	2.8	4.7	0.86	0.52	18.4	Bal.

Note: Values for conventional Inconel 718 are taken from [19].

2.2 | Thermomechanical Fatigue Testing

The TMF tests were conducted in laboratory air under total strain-control using a servo-electric Zwick TMF testing machine as described in previous reports [19, 28]. The specimens were inductively heated using a 5-kW high-frequency generator and a water-cooled copper coil. Cooling was achieved by thermal conduction into the water-cooled grips and to the ambient air. The temperature was measured and controlled using a ribbon-type NiCr-Ni thermocouple (type K) that was wrapped around the center of the specimen's gauge length. All tests used a temperature range of 300°C–650°C to simulate a brief shut-down from service conditions, which are demanding for Inconel 718. The temperature range was selected to allow comparison with TMF results from both conventionally-rolled and PBF-EB Inconel 718 [19].

The temperature rate during both heating and cooling was 5°C s^{-1}, resulting in a triangular waveform with equal ramps (ER) and a cycle time of 140 s. To boost creep–fatigue interaction, some tests included a 10 min dwell time at the peak temperature of 650°C in each cycle. The resulting cycle time in dwell-time (DT) tests was 740 s. A capacitive high-temperature extensometer with 10 mm gauge length was attached to the specimens using alumina rods to measure and control the total strain. During TMF testing, the total strain ε_t is composed of the mechanical strain ε_{me} and the thermal strain ε_{th}. Prior to TMF testing, each specimen was subjected to stress-free thermal cycles to record the time course of ε_{th} . The desired ε_{me} time course was then added to the ε_{th} time course to derive the controlling ε_t time course. The mechanical loading was symmetrical ($R_\varepsilon = -1$) and started at the mean temperature of 475°C. The waveform of ε_{me} was triangular in ER tests and trapezoidal in DT tests. The plastic strain amplitude during TMF testing was measured as half-width of the stress–strain hysteresis loop at the mean stress level. Tested TMF phase relations were IP and OP. Figure 2 shows a schematic of the courses of strain and temperature for the applied cycles.

The tested mechanical strain amplitudes $\varepsilon_{a,me}$ varied between 0.4 and 0.6, resulting in cycles to failure between about 200 and 13 000. The number of cycles to failure, which will be used synonymously with lifetime, was determined by a 10% drop of the stabilized maximum stress [28]. The elastic modulus of the individual specimens was measured prior to TMF testing by elastically cycling the specimens between 0 and approximately 160 MPa.

2.3 | Analysis

Microstructural observation of the initial and post-test microstructure was done by means of scanning electron microscopy (SEM) and transmission electron microscopy (TEM). Specifically, longitudinal sections of the gauge length (prior to and after TMF testing) were observed by a Tescan LYRA 3 XMU FEG-SEM/FIB equipped with an Oxford Instruments Symmetry 2 electron backscatter diffraction (EBSD) detector. SEM operating conditions were 10 kV for SE imaging and 20 kV for EBSD mapping. The overall damage was documented in secondary-electron (SE) imaging and by EBSD on metallographic specimens that underwent a standard metallographic preparation routine consisting of grinding with SiC paper to P1200 and subsequent electropolishing using a Struers LectroPol-5 with an electrolyte of 93.9 vol.% ethanol, 1.4 vol.% nitric acid, and 4.7 vol.% perchloric acid at −15°C/54 V for 6–10 s. Additional post-test characterization of deformation structures employed a JEOL JEM-2100F TEM operated at 200 kV in both parallel-beam (diffraction pattern) and convergent-beam scanning TEM (STEM) bright-field (BF) modes. Oriented TEM foils were prepared by standard electrolytic thinning: ~3 mm-wide plates (cut parallel to the load axis) were ground to 70 µm and thinned in a Struers TenuPol-2 double-jet device using 70 vol.% methanol, 20 vol.% glycerin, and 10 vol.% perchloric acid at −5°C/11 V/~40 mA for 90–120 s, yielding ~70–100 nm-

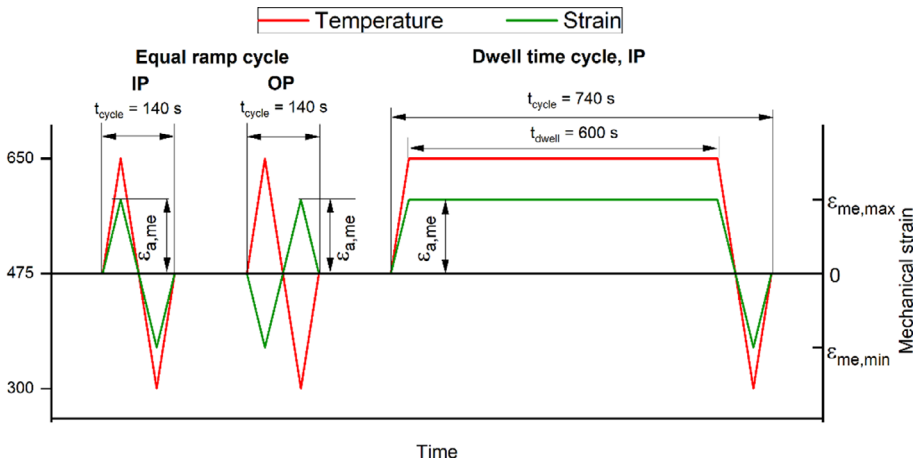

FIGURE 2 | Courses of temperature and strain for the tested cycle and loading types.

thick areas suitable for TEM. To assess the microstructural features, including strengthening precipitates morphology and diameter, as well as grain boundary precipitates from STEM images, VGSTUDIO MAX software by Hexagon was utilized.

3 | Results

3.1 | Unloaded Material in As-Built and Heat-Treated State

Figure 3 shows representative images of the unloaded microstructure of PBF-LB Inconel 718 in the as-built state and after HIP and heat treatment. In the as-built state, the grains exhibit a characteristic melt-pool structure typical of PBF-LB-built alloys. A moderate <001>fiber texture is observed along the building direction, with a maximum multiple of random distribution (MRD) of 3.21. The EBSD-derived {100}, {110}, and {111} pole figures are shown in Figure S1 in the Supporting Information. Within the grains, dislocations form regular cellular and columnar subgrains. Occasional precipitates, which are presumed to be Laves phases, are located in the dislocation cell walls. Larger amounts of the γ' or the γ'' phase could not be found. After HIP and subsequent heat treatment, the grains exhibit neither a melt-pool structure nor a pronounced texture, indicating that recrystallization occurred. There is no dislocation cell structure observable, and, in comparison to the as-built state, the dislocation density appears significantly lower. Consistent with the microstructure of age-hardened conventional Inconel 718, the grains contain finely dispersed disc-shaped γ'' precipitates and occasional larger δ phase discs. The Laves phases appear to have been largely dissolved.

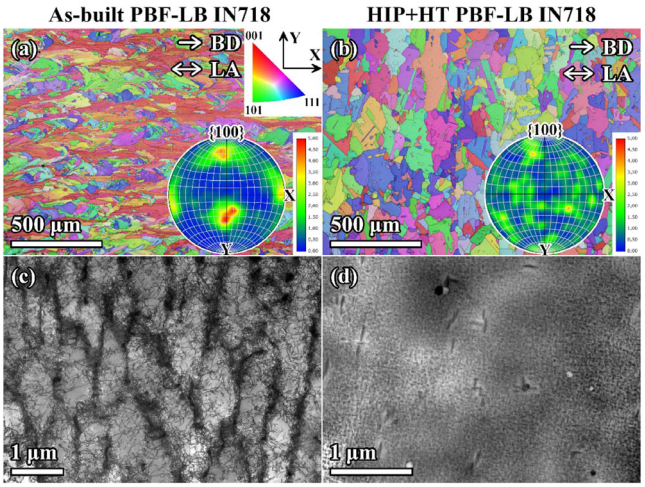

FIGURE 3 | EBSD (IPFX color code) images with {100} pole figures (a,b) and TEM images (c,d) from longitudinal sections of the unloaded microstructure of PBF-LB Inconel 718. (a) and (c), as built-state, (b) and (d) recrystallized state after HIP and heat treatment.

Table 2 summarizes the initial state characteristics of PBF-LB and conventional Inconel 718 specimens. For the grain size measurements, at least 800 grains were considered. For the PBF-LB material, the large difference between mean grain size and area-weighted mean grain size signifies a large range of grain sizes, as can be seen from Figure 3b. The grains are rather irregular in shape and exhibit numerous annealing twins. Near the surface, there is an approximately 15 µm thick fine-grained layer with grain sizes of approximately 10 µm. The surface layer was plastically deformed during machining prior to the HIP and heat treatment. Therefore, finer grains developed during recrystallization. In comparison with the PBF-LB material, the grains in the conventional material are more equiaxed and more polygonal, and the range of grain sizes is smaller [19]. In the heat-treated state, both PBF-LB and conventional Inconel 718 exhibit a γ matrix with finely dispersed disc-shaped γ'' precipitates. The mean length (disc diameter) of the γ'' precipitates in the PBF-LB material is approximately 25% smaller than in the conventional material. The density of all tested specimens was determined by the Archimedes method, using ethanol as the immersion medium. Comparison of the measured values indicates that the PBF-LB specimens already had a high relative density of more than 99.5%, which was then further increased to almost 100% by the HIP treatment. The Vickers hardness of the PBF-LB specimens increased by approximately 50% after the heat treatment, which can be primarily ascribed to the formation of the finely dispersed γ'' precipitates. The hardness values after heat treatment for PBF-LB and conventional material match closely. The elastic modulus values for PBF-LB specimens are approximately 10% lower than those measured for the conventional specimens.

TABLE 2 | Properties of testing materials prior to TMF testing.

	Grain size (after heat treatment) in µm		γ'' diameter in nm	Density in kg m^{-3}		Hardness in HV1		Elastic modulus in GPa	
	Mean	Area-weighted mean		Prior to HIP	After HIP	Prior to heat treatment	After heat treatment	Room temperature	475°C
PBF-LB Inconel 718	42.2	147.8	38.1 ± 11.4	8165 ± 5	8183 ± 19	339.6 ± 18.3	509.3 ± 18.1	198 ± 1.9	171.2 ± 3
Conventional Inconel 718	74.3	148.5	52 ± 3.7		8190 ± 8		494.6 ± 28.1 HV1	218.7 ± 2.9	189.5 ± 2.9

Note: The data for conventional Inconel 718 were already reported in Guth et al. 2026 [19].

3.2 | TMF Lifetime

Figure 4 shows the lifetime results for the various loading conditions, depending on the mechanical strain amplitude. The data of the IP-TMF tests for conventional Inconel 718 were taken from the previous report [19]. For the PBF-LB specimens, the lifetimes under OP ER loading are significantly longer than under IP ER loading. The slope of the OP ER curve is slightly higher than that of the IP ER curve, resulting in OP lifetime approximately 2.7 times longer for $\varepsilon_{a,me} = 0.4\%$ and 4.3 times longer for $\varepsilon_{a,me} = 0.6\%$. For ER cycling, the lifetimes of PBF-LB specimens reach nearly those of conventionally-rolled specimens under both IP and OP conditions. When dwell times are introduced under IP conditions, the lifetime of PBF-LB specimens decreases substantially, particularly at lower mechanical strain amplitudes. For conventional specimens, the lifetime reduction due to dwells is more pronounced at higher mechanical strain amplitudes. As a result, the lifetime difference between PBF-LB and conventional material under IP-TMF loading with dwells is particularly significant at lower mechanical strain amplitudes.

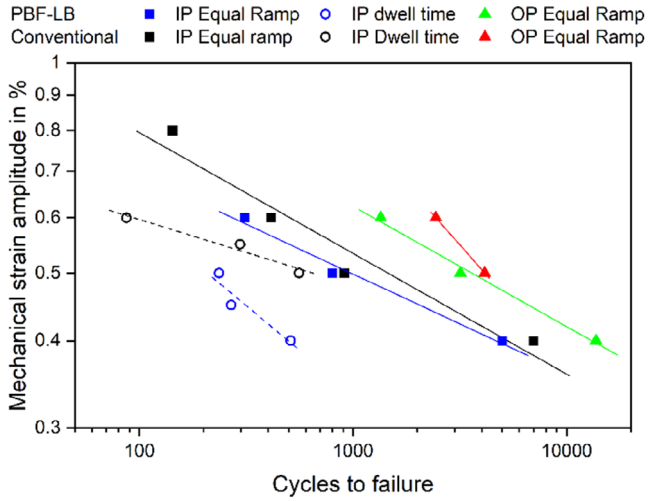

FIGURE 4 | Influence of cycle type and phase angle on the TMF lifetimes of Inconel 718 manufactured by PBF-LB and by conventional rolling. The lifetimes for conventional Inconel 718 under IP loading have already been reported in Guth et al. 2026 [19].

3.3 | Cyclic Deformation Behavior during TMF

Figure 5 presents the stress–strain hysteresis loops of TMF tests with $\varepsilon_{a,\,me} = 0.5\%$ recorded at half of the lifetime for PBF-LB and conventional Inconel 718. For all cycle types, the cyclic deformation behavior of the PBF-LB material closely matches that of the conventional material. A notable difference between the two fabrication methods is the lower plastic strain amplitudes observed in the PBF-LB material, as indicated by narrower hysteresis loops. For a given cycle type and mechanical strain amplitude, PBF-LB specimens consistently exhibited lower plastic strain amplitudes than conventionally-processed specimens throughout their entire fatigue life. The approximately 10% lower elastic modulus of the PBF-LB specimens is reflected in the slightly lower slopes of the elastic branches of the respective loops. For TMF IP DT cycling, the tensile stress during the dwell time at maximum strain relaxes slightly by approximately 5% to 10%, see Figure 5b. Compared to IP ER cycling, IP DT cycling results in higher stress amplitudes and lower plastic strain amplitudes for both the PBF-LB and the conventional material. Since in IP loading, tensile strains occur at higher temperatures than compressive strains, the mean stress is consistently negative. Accordingly, the mean stress in OP tests is positive. For all OP tests on PBF-LB Inconel, the mean stress during cycling remained nearly constant, i.e., the hysteresis loops did not shift to higher tensile stresses.

Figure 6 shows the stress amplitudes with respect to the cycle number for all conducted TMF tests. During TMF-ER cycling, the stress amplitude of PBF-LB Inconel 718 decreases significantly, indicating cyclic softening regardless of the applied strain amplitude or phase angle. Introducing dwells during IP loading reduces the propensity for cyclic softening, resulting in a nearly cyclically neutral behavior of PBF-LB Inconel 718 in IP DT tests. For a given cycle type and strain amplitude, the evolution of the stress amplitude is comparable for PBF-LB and conventional Inconel 718. However, the PBF-LB material exhibits slightly less pronounced cyclic softening.

3.4 | Microstructural Evolution during TMF

Figure 7 shows representative TEM images of the microstructure of TMF-tested PBF-LB specimens. For ER cycling under both IP

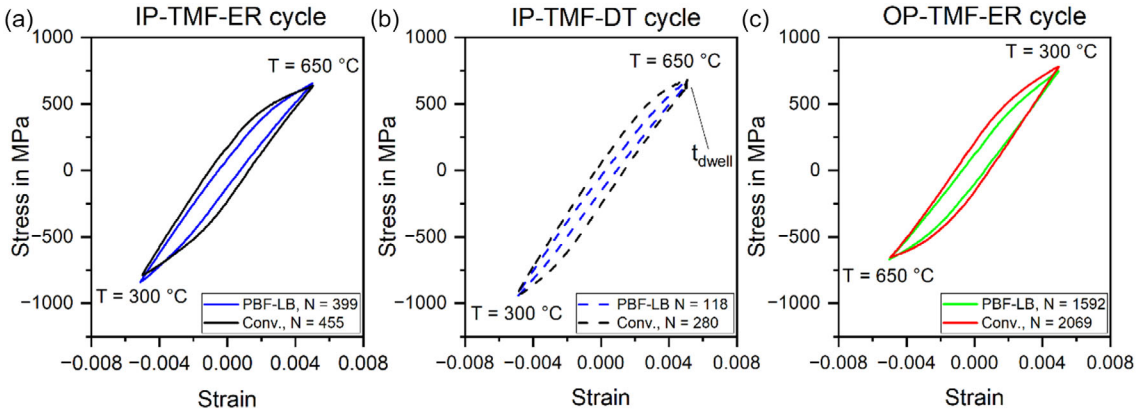

FIGURE 5 | Stress–strain hysteresis loops for PBF-LB and conventional Inconel 718 at half of the lifetime with $\varepsilon_{a,me} = 0.5\%$ for (a) IP-TMF-ER cycling, (b) IP-TMF-DT cycling, and (c) OP-TMF-ER cycling. The loops for conventional Inconel 718 under IP loading have already been reported in Guth et al. 2026 [19].

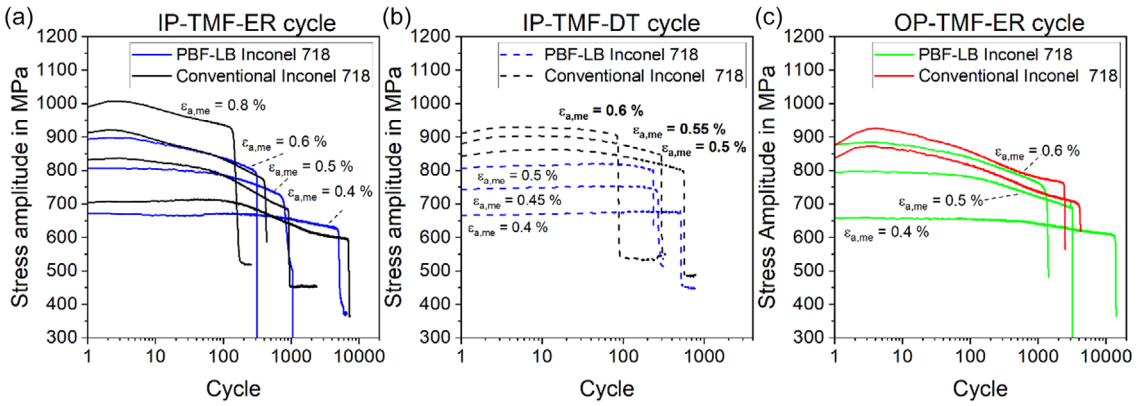

FIGURE 6 | Evolution of the stress amplitude during TMF cycling of Inconel 718 fabricated by PBF-LB and by conventional rolling. (a) IP-TMF-ER cycling, (b) IP-TMF DT cycling, and (c) OP-TMF-ER cycling. The stress amplitudes for conventional Inconel 718 under IP loading have already been reported in Guth et al. 2026 [19].

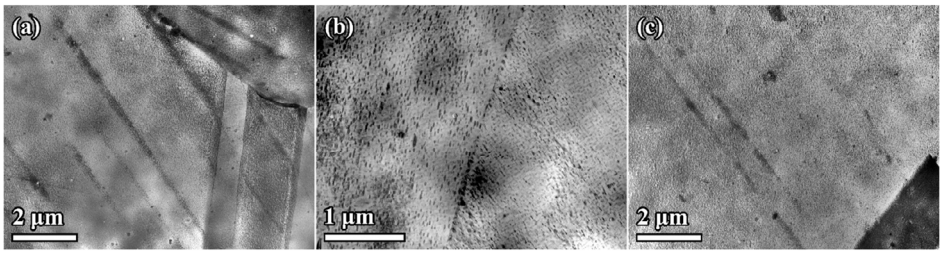

FIGURE 7 | TEM images from PBF-LB Inconel 718 specimens after TMF failure. (a) IP ER loading with $\varepsilon_{a,me} = 0.6\%$, $N_f = 312$, (b) IP DT loading with $\varepsilon_{a,me} = 0.4\%$, $N_f = 511$, and (c) OP ER loading with $\varepsilon_{a,me} = 0.6\%$, $N_f = 1349$.

and OP conditions, dislocations have localized into slip bands. Generally, no discernible differences were observed in the microstructure after ER cycling with IP and OP conditions. Twins, as displayed in all images of Figure 7, were also frequently found in the initial state. Therefore, they are presumably annealing twins, which developed during the HIP treatment and not during TMF testing. After dwell time cycling, no dislocation slip bands were observed. Based on the TEM observations, the morphology of the γ″ precipitates appears unchanged during TMF cycling. Measurements of the γ″ precipitate sizes after TMF cycling with dwell times for more than 500 cycles resulted in mean lengths (disc diameters) of 40.2 ± 12 nm and an aspect ratio of approximately 0.4, which is very close to the initial state.

3.5 | TMF Damage Analysis

Figure 8 presents images from longitudinal sections of PBF-LB Inconel 718 specimens after TMF cycling with typical fatigue cracks. Under IP loading, cracks grow predominantly intergranular along the grain boundaries, while transgranular cracking was also observed. In many cases, the cracks appear to be internal without connection to the surface. Introducing dwell times had no significant effect on the crack appearance after IP loading. Under OP loading, fatigue cracks start mainly from the surface and grow transgranularly. OP cracks exhibit a sharp morphology and grow primarily perpendicular to the loading direction. Under all loading conditions, the grain boundaries in the fine-grained surface layer oxidized severely, as can be seen in Figure 8b. For conventional Inconel 718 featuring no fine-grained surface layer, near-surface grain boundary oxidation was much less pronounced.

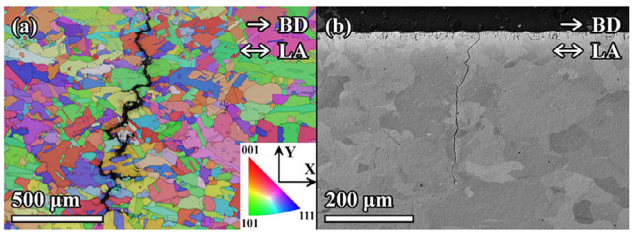

FIGURE 8 | Representative damage after TMF loading of PBF-LB Inconel 718. (a) EBSD image (IPFX color code) after IP-TMF-ER loading with $\varepsilon_{a,me} = 0.6\%$, $N_f = 312$. (b) SE image after OP-TMF-ER loading with $\varepsilon_{a,me} = 0.6\%$, $N_f = 1349$.

Internal grain boundary cracks could be observed after both IP and OP testing. Figure 9 shows representative examples. Under IP loading, the angle between internal grain boundary cracks and the loading direction is generally large, whereas under OP loading, it is comparatively small. The bright particles visible in both images of Figure 9 are mainly Nb-carbides. After the OP loading of conventional Inconel 718, no intergranular cracks under a low angle to the loading direction could be observed.

4 | Discussion

4.1 | Microstructure and Deformation Behavior

The as-built PBF-LB microstructure recrystallized presumably during HIP at 1120°C, which was the highest temperature during postprocessing, see Figure 3. Recrystallization of PBF-LB Inconel

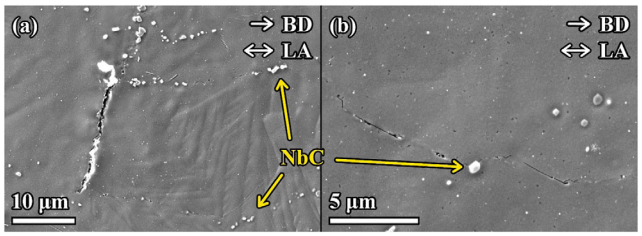

FIGURE 9 | Internal grain boundary damage after TMF loading of PBF-LB Inconel 718. (a) grain boundary crack under high angle to the loading direction after IP-TMF-ER loading with $\varepsilon_{a,me} = 0.5\%$, $N_f = 798$. (b) grain boundary crack under low angle to the loading direction after OP-TMF-ER loading with $\varepsilon_{a,me} = 0.6\%$, $N_f = 1349$.

718 during HIP with similar resulting grain structures as in this study has been observed by Aydinöz et al. at 1150°C [21] and by Sanchez-Camargo et al. at 1200°C [22]. In this study, HIP at 1120°C led to recrystallization, whereas Sonntag et al. reported no recrystallization following solution annealing at 1065°C [25]. Accordingly, the approximate onset temperature for recrystallization of PBF-LB Inconel 718 can be found in the range between 1065°C and < 1120°C and depends presumably also on the HIP pressure, the annealing time, and the PBF-LB building parameters. Considering the already high relative density in the as-built state, HIP may be omitted when the as-built grain structure is to be conserved. Interestingly, Inconel 718 fabricated by PBF-EB did not recrystallize upon identical HIP at 1120°C [28]. In contrast to PBF-LB Inconel 718, as-built PBF-EB Inconel 718 contains a relatively low dislocation density [29], as the cooling rates during PBF-EB are much lower, resulting in lower thermal stresses and reduced dislocation nucleation [30]. Moreover, the higher manufacturing temperatures during PBF-EB promote continuous recovery. Consequently, the driving force for recrystallization is reduced, and the onset temperature increased.

Despite slight differences in grain structure and γ″ precipitate size between PBF-LB and conventionally-processed Inconel 718, both materials show similar initial hardness, hysteresis loops, and stress amplitude evolution under TMF loading. The slightly lower plastic strain amplitudes of PBF-LB Inconel 718 can be explained by its approximately 10% lower elastic modulus, in combination with a flow stress comparable to that of conventional Inconel 718. The cyclic softening observed in the TMF-ER tests was similarly reported by Zou et al. [27] and is also typical for γ″-strengthened conventional Inconel 718 under TMF loading with ER [8, 9]. As for conventional Inconel 718 [19], we attribute the cyclic softening observed in TMF-ER tests of PBF-LB material to γ″ precipitate shearing along the dislocation slip bands (Figure 7) as proposed by Founier and Pineau [15]. Given the lower plastic strain amplitudes in PBF-LB Inconel 718, we assume that fewer slip bands form and fewer γ″ precipitates are sheared, which eventually leads to less pronounced cyclic softening compared to conventional Inconel 718. Introducing dwell times in IP-TMF tests prevented cyclic softening for PBF-LB material, which aligns with the fact that no dislocation slip bands were found after IP-TMF DT testing. Similar tendencies were found for conventional Inconel 718 [19]. It appears that dwell times prevent dislocations from localizing into slip bands. The likely reason for this is recovery processes due to intensified cross slip and non-conservative dislocation movements (climb), leading to a reduced dislocation density. The tensile stress relaxation during the dwell time—amounting to approximately 5% to 10%—is comparatively minor, reflecting the good resistance to static creep of both PBF-LB and conventional Inconel 718 at 650°C. The good creep resistance is also responsible for the nearly constant mean stress during OP ER cycling. Accordingly, creep–fatigue interaction in the form of increasing tensile mean stresses plays only an insignificant role in OP ER loading [10]. From the results can be concluded that the cyclic deformation behavior of recrystallized PBF-LB Inconel 718 under TMF loading is very similar to that of conventional Inconel 718, when identical heat treatments were applied.

4.2 | TMF Damage, Creep–Fatigue Interaction and Lifetime

The TMF damage is predominantly intergranular in IP loading and transgranular in OP loading, which is typical for Inconel 718 in both conventional [8, 9] and PBF-LB [27] form. For both IP and OP loading, initial intergranular cracks form due to grain boundary sliding in the high temperature regime of the TMF cycles. The orientation of the grain boundary cracks with respect to the loading direction can be explained with the model of Taira et al. [5]. In their study on type 304 austenitic steel, Taira et al. marked grain boundaries using intersecting lines and observed the relative displacement of these markers, attributed to grain boundary sliding under TMF loading with both IP and OP phase angles. Since grain boundaries slide only at elevated temperatures, grain boundary sliding is activated under external tensile stress during IP loading and under external compressive stress during OP loading. As a result, grain boundary cracks in IP loading typically form at high angles to the external load, whereas in OP loading, the cracks tend to exhibit low angles relative to the loading direction [5]. This behavior can be seen from Figure 9 and was similarly found for the Ni-based superalloy Inconel 617 [7] and the Co-based superalloy Haynes 188 [6]. However, grain boundary cracks with orientations dependent on the TMF phase angle have, to the best of our knowledge, not been reported for Inconel 718. Particularly, the comparative OP tests on conventional Inconel 718 conducted in this study did not produce intergranular cracks. This indicates that the PBF-LB Inconel 718 tested here is more susceptible to grain boundary sliding than conventional Inconel 718. After initiation, the grain boundary cracks at high angles to the loading direction in IP loading are stressed by the alternating external load. Therefore, they can grow along grain boundaries and coalesce with other nearby grain boundary cracks, which eventually results in large intergranular damage as shown in Figure 8a [7]. In OP loading, the grain boundary cracks at low angle to the loading direction are barely subjected to the external load and grow only due to grain boundary sliding. As a result, they remain relatively short, and the overall damage under OP loading is mainly transgranular, see Figure 8b [7].

The observed shorter lifetimes in IP ER tests compared to OP ER tests (Figure 4) suggest that intergranular crack propagation in IP loading is faster than transgranular crack propagation in OP loading. We assume that the observed significant lifetime reduction in IP DT tests (Figure 4) results from the sustained high tensile stress during the dwell periods, which promotes intergranular cracking through grain boundary sliding. This suggests that the previously mentioned good resistance against static creep may, in fact, be

detrimental to the creep-fatigue performance of PBF-LB Inconel 718. In comparison with the TMF results (IP-TMF-ER and OP-TMF-ER) of Zou et al., who tested PBF-LB Inconel 718 in the non-recrystallized state after solution annealing at 980°C and subsequent two-stage aging, the strain-life curves observed in this study show a markedly lower slope [27]. In particular, the material tested here reveals longer lifetimes at lower mechanical strain amplitudes, while the material tested by Zou et al. exhibits longer lifetimes at higher mechanical strain amplitudes under both IP and OP conditions [27]. The results highlight the impact of post-manufacturing treatments on the TMF lifetime behavior of PBF-LB Inconel 718 and suggest that HIP, resulting in recrystallization, is favorable for long time service at lower mechanical strain amplitudes.

As previously noted, the PBF-LB material investigated in this study exhibits a fine-grained surface layer resulting from HIP treatment following machining. This microstructural feature is generally considered susceptible to intergranular damage and could contribute to the materials' low resistance to tensile dwell loading and creep–fatigue interaction. Since the intergranular damage observed after both IP ER and IP DT loading occurred primarily in the bulk, the contribution of the fine-grained surface layer to the creep-fatigue resistance cannot be conclusively assessed and is therefore presumed to be secondary. The fact that PBF-LB specimens reached nearly the lifetimes of conventional specimens under IP ER loading (Figure 3) supports this interpretation. Under OP ER loading, the pronounced grain boundary oxidation in the fine-grained surface layer may have led to earlier crack initiation. This may contribute to the lower lifetimes of PBF-LB specimens in such tests when compared to conventional specimens, although both stress amplitudes and plastic strain amplitudes are lower for the PBF-LB specimens. In summary, the presence of a fine-grained surface layer is presumably not beneficial for the TMF resistance and HIP should be preferably applied prior to final machining. As this sequence reflects typical industrial practice, the specimens tested here are not fully representative of real components, which limits the direct transferability of the lifetime data. Nevertheless, any resulting deviation in lifetime is expected to be conservative.

4.3 | Impact of Grain Boundary Precipitates on Creep-Fatigue Resistance

Notably, introducing dwell times under IP-TMF loading conditions reduced the lifetimes more significantly for PBF-LB Inconel 718 than for conventional Inconel 718 (see Figure 4). In contrast, a previous study on PBF-EB Inconel 718 reported longer lifetimes in some dwell time tests compared with ER tests [19]. Neither PBF-EB nor conventional Inconel 718 exhibited severe signs of grain boundary sliding [19] as observed for the PBF-LB Inconel 718 tested here. To further investigate the susceptibility to grain boundary sliding, differences between the grain boundaries of conventional, PBF-LB and PBF-EB Inconel 718 were observed using TEM. Details on the PBF-EB samples can be found in a previous report [28]. Representative images are shown in Figure 10. For conventional Inconel 718, the grain boundaries are decorated with finely dispersed carbides of type NbC. Both PBF-LB and PBF-EB Inconel 718 exhibit needle- or disc-shaped δ precipitates along and across the grain boundaries; however, in PBF-EB Inconel 718, these precipitates are typically larger and more numerous. In PBF-LB Inconel 718, there are sizeable grain boundary segments without any precipitates.

The results suggest that the lack of grain boundary precipitates in PBF-LB Inconel 718 makes it susceptible to grain-boundary sliding and, consequently, to creep–fatigue interaction [26]. Accordingly, the material investigated here may be of limited suitability for applications characterized by sustained tensile dwells. Interestingly, in IP tests without dwell times, the PBF-LB material reaches nearly the lifetimes of conventionally-rolled material. This emphasizes the importance of near-service creep-fatigue testing when components are to be subjected to TMF in combination with steady state loading at elevated temperatures. Zhao et al. pointed out that NbC carbides do not form during PBF-LB processing of Inconel 718 because of solute trapping during rapid solidification [31]. Ghaemifar et al. reported that NbC carbides form in PBF-LB Inconel 718 upon annealing at temperatures above 1000°C [32]. Figure 9 shows that, in the PBF-LB Inconel 718 alloy tested here, some NbC carbides are located along grain boundaries. These carbides likely formed during either HIP at 1120°C or solution annealing at 1065°C. However, it appears that not enough NbC carbides are present to effectively prevent grain boundary sliding. The δ phase precipitates in PBF-LB Inconel 718 at temperatures between approximately 800°C and 950°C [33]. This suggests that the δ precipitates have formed during controlled furnace cooling from the solution annealing temperature of 1065°C to the first age hardening temperature of 718°C. This cooling step was realized with a temperature rate of 4°C min^{-1}, resulting in a total ramp time of approximately 87 min. However, the period in the δ precipitation regime was apparently too short to form sufficient δ precipitates to impede grain boundary sliding. Popovich et al. performed an annealing treatment at 850°C on PBF-LB Inconel 718, followed by a two-step aging at 720°C and 621°C, which led to δ phase precipitation along grain boundaries. They further found that this heat treatment increased the lifetime under IP-TMF-DT conditions with $T = 350°C–650°C$ and tensile dwells of 300 s considerably, and explained it with the δ phase preventing grain boundary sliding [26]. For $\varepsilon_{a,me} = 0.45\%$, the material tested by Popovich et al.

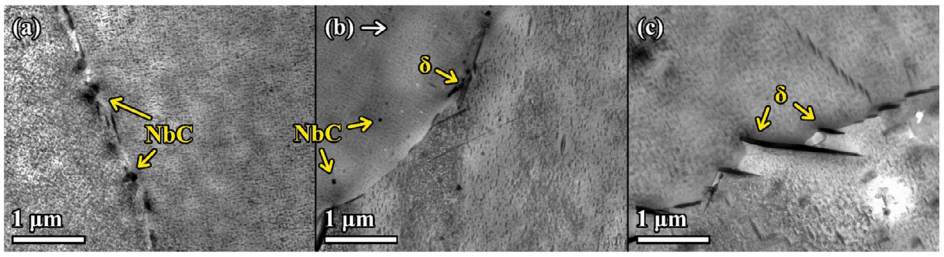

FIGURE 10 | Representative grain boundary precipitates in Inconel 718 fabricated by: (a) conventional rolling, (b) PBF-LB, and (c) PBF-EB.

yielded a TMF lifetime of 1246 cycles [26], whereas the material tested here reached only 269 cycles. Although we tested with dwell periods twice as long (600 s) and the fine-grained surface layer may also have had an influence, the results indicate that a sufficient presence of grain boundary precipitates—either NbC or δ phase—appears to be important for the creep-fatigue resistance of PBF-LB Inconel 718. Accordingly, further studies should investigate whether and how optimized heat treatments can enhance the creep-fatigue resistance of PBF-LB Inconel 718.

5 | Summary and Conclusions

Strain-controlled TMF experiments in a temperature range of 300°C–650°C under in-phase and OP conditions have been performed on additively manufactured PBF-LB Inconel 718. In some in-phase TMF tests, tensile dwell times of 600 s were introduced at the maximum temperature of 650°C to induce severe creep–fatigue interaction. The main findings can be summarized as follows:

1. HIP at 1120°C leads to recrystallization of the as-built grain structure. After a standard solution annealing and two stage aging treatment, the PBF-LB material exhibits a γ/γ'' microstructure typical for Inconel 718. The resulting cyclic deformation behavior under TMF loading closely matches that of conventionally rolled Inconel 718.
2. In TMF tests without dwell times, the PBF-LB Inconel 718 reaches almost the lifetimes of conventionally rolled Inconel 718. Introducing dwell times significantly reduces the lifetimes of PBF-LB Inconel 718, particularly at lower mechanical strain amplitudes. Accordingly, the material investigated here appears to be less suitable for applications involving severe creep–fatigue interaction.
3. Microstructural observations indicate that the reason for the poor creep-fatigue resistance of the tested PBL-LB material is a lack of either δ precipitates or NbC carbides along grain boundaries. This appears to facilitate grain boundary sliding, resulting in severe intergranular crack propagation.

Author Contributions

Stefan Guth: conceptualization (lead), investigation (equal), project administration (lead), supervision (equal), visualization (equal), writing – original draft (lead). **Tomáš Babinský**: investigation (supporting), visualization (equal), writing – review & editing (equal). **Jan Lars Riedel**: investigation (supporting), writing – review & editing (supporting). **Wen Hao Kan**: resources (equal), writing – review & editing (supporting). **Aijun Huang**: resources (equal), supervision (supporting), writing – review & editing (supporting). **Martin Heilmaier**: resources (equal), supervision (equal), writing – review & editing (equal). **Ivo Šulák**: investigation (equal), resources (equal), supervision (equal), writing original draft (supporting), writing – review & editing (equal).

Acknowledgments

Ivo Šulák acknowledges the support of the Czech Academy of Sciences under the framework of the Lumina quaeruntur project. The authors thank the unknown reviewers for their valuable input.

Open Access funding enabled and organized by Projekt DEAL.

Funding

This work was supported by the Czech Academy of Sciences under the framework of the Lumina quaeruntur project.

Data Availability Statement

The data that support the findings of this study are available from the corresponding author upon reasonable request.

References

1. D. A. Boismier and H. Sehitoglu, "Thermo-Mechanical Fatigue of Mar-M247: Part 1—Experiments," *Journal of Engineering Materials and Technology* 112 (1990): 68.

2. H.-J. Christ, "Effect of Environment on Thermomechanical Fatigue Life," *Materials Science and Engineering: A* 468–470 (2007): 98.

3. S. Guth, S. Doll, and K.-H. Lang, "Influence of Phase Angle on Lifetime, Cyclic Deformation and Damage Behavior of Mar-M247 LC under Thermo-Mechanical Fatigue," *Materials Science and Engineering: A* 642 (2015): 42.

4. I. Šulák and K. Obrtlík, "Thermomechanical and Isothermal Fatigue Properties of MAR-M247 Superalloy," *Theoretical and Applied Fracture Mechanics* 131 (2024): 104443.

5. S. Taira, M. Fujino, and M. Yoshida, "Grain Boundary Sliding in Isothermal and Thermal Fatigue of Type 304 Stainless Steel," *ISIJ Int* 19 (1979): 191.

6. S. Kalluri and G. Halford, "*Thermomechanical Fatigue Behavior of Materials*," (ASTM International,1993): 126.

7. S. Guth and K.-H. Lang, "An Approach to Lifetime Prediction for a Wrought Ni-Base Alloy under Thermo-Mechanical Fatigue with Various Phase Angles between Temperature and Mechanical Strain," *International Journal of Fatigue* 99 (2017): 286.

8. W. Deng, J. Xu, Y. Hu, Z. Huang, and L. Jiang, "Isothermal and Thermomechanical Fatigue Behavior of Inconel 718 Superalloy," *Materials Science and Engineering: A* 742 (2019): 813.

9. J. Sun and H. Yuan, "Life Assessment of Multiaxial Thermomechanical Fatigue of a Nickel-Based Superalloy Inconel 718," *International Journal of Fatigue* 120 (2019): 228.

10. M. Sirrenberg, D. Bürger, S. Guth, et al., "Out-of-Phase Thermomechanical Fatigue of a Single Crystal Ni-Base Superalloy," *Materials Science and Engineering: A* 910 (2024): 146851.

11. H. Zhou, H. Harada, Y. Ro, and I. Okada, "Investigations on the Thermo-Mechanical Fatigue of Two Ni-Based Single-Crystal Superalloys," *Materials Science and Engineering: A* 394 (2005): 161.

12. S. Guth, R. Petráš, V. Škorík, et al., "Influence of Dwell Times on the Thermomechanical Fatigue Behavior of a Directionally Solidified Ni-Base Superalloy," *International Journal of Fatigue* 80 (2015): 426.

13. I. Šulák and K. Obrtlík, "The Effect of Dwell on Thermomechanical Fatigue Behaviour of Ni-Base Superalloy Inconel 713LC," *International Journal of Fatigue* 166 (2023): 107238.

14. H. F. Merrick, "The Low Cycle Fatigue of Three Wrought Nickel-Base Alloys," *Metall Trans* 5 (1974): 891.

15. D. Fournier and A. Pineau, "Low Cycle Fatigue Behavior of Inconel 718 at 298 K and 823 K," *Metall Trans A* 8 (1977): 1095.

16. K. Kuwabara, A. Nitta, and T. Kitamura, *Proceedings of ASME International Conference on Advances in Life Prediction Methods*, (1983), 131.

17. S.-H. Sun, Y. Koizumi, T. Saito, et al., "Electron Beam Additive Manufacturing of Inconel 718 Alloy Rods: Impact of Build Direction on Microstructure and High-Temperature Tensile Properties," *Additive Manufacturing* 23 (2018): 457.

18. C. Körner, H. Helmer, A. Bauereiß, and R. F. Singer, "Tailoring the Grain Structure of IN718 during Selective Electron Beam Melting," *MATEC Web of Conferences* 14 (2014): 08001.

19. S. Guth, T. Babinský, S. Antusch, A. Klein, D. Kuntz, and I. Šulák, "Comparison of Electron-Beam-Melted and Conventionally Rolled Inconel 718 under Thermomechanical Creep-Fatigue Loading," *International Journal of Fatigue* 202 (2026): 109238.

20. E. Hosseini and V. A. Popovich, "A Review of Mechanical Properties of Additively Manufactured Inconel 718," *Additive Manufacturing* 30 (2019): 100877.

21. M. E. Aydinöz, F. Brenne, M. Schaper, et al., "On the Microstructural and Mechanical Properties of Post-Treated Additively Manufactured Inconel 718 Superalloy under Quasi-Static and Cyclic Loading," *Materials Science and Engineering: A* 669 (2016): 246.

22. C. Sanchez-Camargo, Y. Nadot, J. Cormier, et al., "Role of Defects and Microstructure on the Fatigue Durability of Inconel 718 Obtained by Additive Layer Manufacturing Route," *Fatigue & Fracture of Engineering Materials & Structures* 46 (2023): 4678.

23. D. Deng, R. L. Peng, and J. Moverare, "A Comparison Study of the Dwell-Fatigue Behaviours of Additive and Conventional IN718: The Role of Dislocation Substructure on the Cracking Behaviour," *Materials Science and Engineering: A* 797 (2020): 140072.

24. A. Kaletsch, S. Qin, and C. Broeckmann, "Influence of Different Build Orientations and Heat Treatments on the Creep Properties of Inconel 718 Produced by PBF-LB," *Materials* 16 (2023): 4087.

25. N. Sonntag, B. Piesker, L. A.Ávila Calderón, et al., "Tensile and Low-Cycle Fatigue Behavior of Laser Powder Bed Fused Inconel 718 at Room and High Temperature," *Advanced Engineering Materials* 26 (2024): 2302122.

26. V. A. Popovich, E. V. Borisov, V. Heurtebise, T. Riemslag, A. A. Popovich, and V. Sh. Sufiiarov, *in TMS. 2018 147th Annual Meeting & Exhibition Supplemental Proceedings (Ed: T.M. & Materials Society Metals)* (Cham: Springer International Publishing, 2018), 85.

27. C. L. Zou, J. C. Pang, W. B. Li, et al., "Thermo-Mechanical Fatigue Behavior and Life Prediction of Selective Laser Melted Inconel 718," *Materials Science and Engineering: A* 919 (2025): 147502.

28. S. Guth, T. Babinský, S. Antusch, A. Klein, D. Kuntz, and I. Šulák, "Creep–Fatigue Interaction of Inconel 718 Manufactured by Electron Beam Melting," *Advanced Engineering Materials* 25 (2023): 2300294.

29. S. Goel, H. Mehtani, S.-W. Yao, I. Samajdar, U. Klement, and S. Joshi, "As-Built and Post-Treated Microstructures of an Electron Beam Melting (EBM) Produced Nickel-Based Superalloy," *Metall Mater Trans A* 51 (2020): 6546.

30. G. Wang, H. Ouyang, C. Fan, et al., "The Origin of High-Density Dislocations in Additively Manufactured Metals," *Materials Research Letters* 8 (2020): 283.

31. Y. Zhao, K. Li, M. Gargani, and W. Xiong, "A Comparative Analysis of Inconel 718 made by Additive Manufacturing and Suction Casting: Microstructure Evolution in Homogenization," *Additive Manufacturing* 36 (2020): 101404.

32. S. Ghaemifar and H. Mirzadeh, "Precipitation Kinetics of Niobium Carbide (NbC) during Homogenization Heat Treatment of Additively Manufactured Inconel 718 Superalloy," *Journal of Materials Research and Technology* 25 (2023): 1774.

33. W. Huang and Z. Wang, "Isothermal Solid-State Transformations of Inconel 718 Alloy Fabricated by Selective Laser Melting," *Advanced Engineering Materials* 23 (2021): 2000982.

Supporting Information

Additional supporting information can be found online in the Supporting Information section. **Supporting Fig. S1**: {100}, {110}, and {111} pole figures of the as-built (a) and hot-isostatically pressed and heat-treated PBF-LB Inconel 718. While the as-built state exhibits a moderate fiber texture along the build direction, there is no pronounced texture after the heat treatment.